In-situ investigation of salt precipitation dynamic induced by gas flow-through drying using simultaneous Neutron and X-ray dual-beam Radiography.

Matthieu Mascle[*1]*, Olivier Lopez*[2]*, Herve Deschamps*[1]*, Lars Rennan*[2]*, Nicolas Lenoir*[3,4]* , Alessandro Tengattini*[3,4]* , Souhail Youssef*[1]

[1]IFP Energies Nouvelles, Rueil-Malmaison, France
[2]Equinor ASA, Trondheim, Norway
[3]Univ. Grenoble Alpes, CNRS, Grenoble INP, 3SR, Grenoble, France
[4]Institut Laue-Langevin (ILL), Grenoble, France

Abstract. In this work, a new dual beam monitoring technique is presented to demonstrate its interest to investigate the salt precipitation dynamics induced by gas flow-through drying. It consists of imaging simultaneously a coreflood using both Neutron and X-ray beams. A method to calibrate and process the two signals is presented. It takes advantage of the difference of attenuation pattern between the two beams to quantify the different phase saturations and composition as well as the reduction of porosity caused by salt precipitation. A set of experiments has been conducted at the NeXT-Grenoble beamline of the Institut Laue-Langevin facilities (ILL, France). Experiments were conducted on an homogeneous rock sample of Bentheimer sandstone using dry nitrogen and a 100g/L KBr brine. The two first experiments aimed to calibrate the dual monitoring for the different phases. The last two experiments have been conducted with a brine capillary contact maintained at the gas outlet. Experimental data have given new insight to understand the organization of the three phases (the brine, the gas and the precipitated salt) when a salt bank is formed in the sample. The quantity of salt that accumulates allows to estimate the flow rate of brine pumped through the capillary contact to compensate the brine evaporation in the gas phase. Observations have shown that a reduction of the initial porosity in some sections of the sample by 13-15% was enough to trigger a gas draw-down characterized by the migration of the salt toward the gas inlet. In some conditions (low gas inlet pressure for example), the rise of the water can be fast enough to form a second salt bank higher in the sample. It has been observed that the formation of the second salt bank could spread the precipitated salt in a less damaging configuration for the gas flow, triggering a phase of gas build-up characterized by the withdrawal of the water. These phases of gas draw-down and build-up can alternate until the sample clogging.

* Corresponding author: matthieu.mascle@ifpen.fr

1. Introduction

The injection of a gas phase through a water saturated porous medium can reduce the saturation above the residual water saturation (Swi) reached after a viscous displacement, by evaporation mechanisms. In the presence of brine, this process can induce salt crystallization and precipitation within the porous medium. The salt precipitation has been investigated in many studies, both experimentally [1–3] and numerically [4–6]. These studies aim to understand the physical and chemical interplay between the gas injection, capillary forces and the porous structure. They showed that the drying rate is proportional to the gas velocity and that any dissolved salt in the water can be transported by capillary flows induced by drying and can even accumulate near the injection surface. The permeability can then be reduced by pore clogging. They conclude that all these mechanisms must be included in models to calculate the near wellbore permeability and porosity changes with time, in order to correctly determine the well injectivity. Yet calibrating such a multi-parameter model is not straightforward and requires advanced experimental investigation to properly quantify the key parameters such as local saturation and salt concentration as well as the porosity reduction or precipitated salt quantity [1, 7, 8]

In a previous study [1] a comprehensive experimental investigation of the effect of gas flow in a sandstone sample initially saturated with water or brine using X-ray radiography has been presented. This study has qualitatively shown the impact of brine capillary contact on the accumulation of salt within the sample during dry gas injection. However, following Beer-Lambert law, X-ray intensity is attenuated by all crossed materials. The measured X-ray contrast is therefore sensitive to all material variations including the water saturation and the salt concentration. X-ray monitoring is not capable by itself to de-correlate and quantify the evolution of local water saturation, salt concentration and precipitate salt quantities.

To overcome this limitation, we introduce in this work a new in-situ monitoring instrument named NeXT-Grenoble and located at Institut Laue-Langevin (ILL, France) [9]. It consists in imaging simultaneously, by radiography, a sample using both Neutron and X-ray beams. We take advantage of the difference in attenuation characteristics of Neutron and X-ray [10]. Indeed, while X-ray is mainly sensitive to material electronic density, Neutron will mainly interacts with atomic nuclei (if magnetic interaction is excluded). There is no straightforward relation between Neutron attenuation coefficient and the material density, while X-ray attenuation coefficients globally increase with the electronic density. For example, Neutron has a very high scattering cross section for hydrogen while chemical element like Bromine (Br), which considerably attenuates X-ray, will be almost transparent to Neutron. A state-of-the-art equipment designed for in-situ coreflood experimentation was used on NeXT-Grenoble to capture the dynamic of salt precipitation induced by gas flow-through drying. The experiments were conducted using a homogeneous rock sample of Bentheimer sandstone. First, the dry-out is conducted with deionized water to

characterize the dynamic without salt precipitation. The same experiment is repeated with a KBr brine water to evaluate when salt precipitation occurs. Finally, the last experiments are conducted with the KBr brine and a capillary contact maintained at the core outlet. This experiment is repeated with two gas injection scenarios: a high and low gas pressure gradient.

The two first experiments aimed to construct and calibrate a method to compute the different phases from the Neutron and X-ray monitoring. It is then applied to monitor the experiments conducted with the capillary contact. The dual monitoring allowed to separately quantify the dissolved and precipitated salt. The latter can be interpreted in terms of porosity reduction.

2. Materials and methods

2.1 Fluids and sample properties

Experiments have been conducted on a homogeneous Bentheimer sandstone of length and diameter L = 2.0 cm and D = 9.32 mm. The sample exhibits high porosity and permeability, measured to ϕ = 23% and K = 1500mD. Its pore-volume is measured to PV = 0.31cc. X-ray and Neutron radiographies of the sample are showed in **Fig. 1** when saturated with nitrogen (N_2).

Three different fluids have been used to perform the experiments: dry nitrogen N_2 for the gas phase, deionized water for the first experiment and a 100g/l KBr brine (this salt concentration is referred as C_o). KBr salt was used for its high electronic density, giving a good X-ray contrast with the gas, and its low Neutron attenuation. Experiments are conducted at ambient temperature (24°C +/- 1°C). KBr solubility in deionized water is estimated to 650g/l for these conditions.
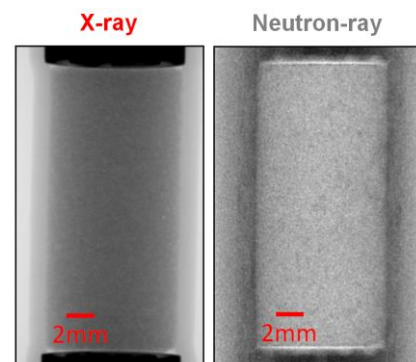

Fig. 1 : X-ray and Neutron-ray radiographies of the Bentheimer rock sample. X-ray and Neutron-ray projections were acquired respectively at a pixel resolution of 40 μm and 15 μm.

2.2 Experimental set-up

The experimental set-up used in this study is shown in **Fig. 2**. Nitrogen is injected from the top at a constant pressure using a downstream pressure regulator. Gas flow rate is monitored using a Coriolis mass flowmeter. Brines (either deionized water or KBr brine) are injected using an Isco-pump. The confining pressure is set to 10bars using deuterated water to be less attenuating to Neutrons compared to normal water, and a 1mm thick perfluoro-

elastomer (FFKM) sleeve. All tubing are connected to a Hassler type cell. The main imaged components of the cell are presented in **Fig. 3**. The cell was designed to bear more than 15bars while being transparent to X-ray and Neutrons. The cell body is composed of a 2mm thick Teflon cylinder, to mitigate both Neutron activation and attenuation. The cell is equipped from each side with three connections (inlet, outlet and static line for the pressure transducer). The inlet/outlet pressures and differential pressure (dP) is measured using a Keller differential pressure sensor. A data acquisition system was used to monitor the pressure, mass flow and temperature. Finally, the set-up was installed in dedicated radiography facility equipment for in-situ saturation monitoring.
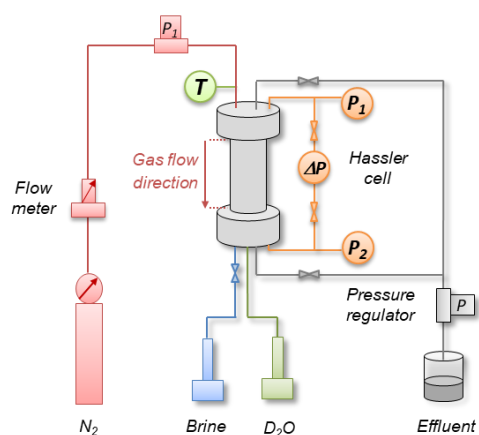

Fig. 2. Overview of the experimental set-up.

For all dry-out tests, the sample is set vertically, with the gas injected from the top of the plug and the water from the bottom. The capillary contact (for the experiments 3 and 4) is maintained by sweeping the bottom of the plug. For the 2D plots, the core axis is normalized as follow: x = 0 refers to the bottom, x = L refers to the top.
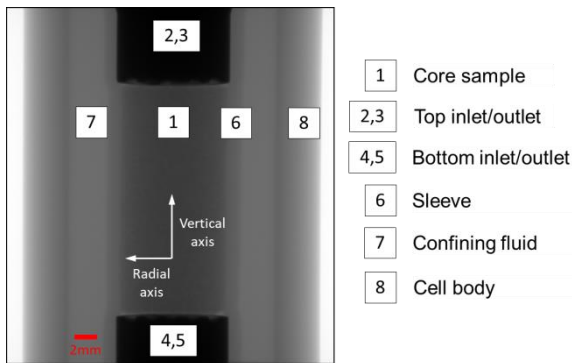

Fig. 3: X-ray Radiography showing the Hassler injection cell.

2.3 Experimental procedure

The four dry-out experiments are conducted using the same injection procedure:

1- Saturating the sample with the brine by injecting from the bottom inlet and opening the top outlet (the bottom outlet and top inlet are closed). To ensure a full saturation, a back pressure of 7bars is imposed after water breakthrough to compress and produce the trapped gas.

2- Opening the bottom outlet and top inlet and closing the top outlet. The water injection is maintained for allowing a sweeping of the bottom face of the sample.

3- After lowering the pore pressure to the atmosphere, the gas is injected at a constant pressure.

4- The sample is finally cleaned by injecting deionized water and increasing the back pressure until the reference X-ray attenuation is reached.

2.4 Dual beam in-situ monitoring

Dynamic in-situ monitoring is performed using the NeXT-Grenoble station recently designed at ILL [9]. It is composed of the dual Neutron and X-ray beams, simultaneously monitoring the sample from a different angle (see illustration **Fig. 4**). A nuclear reactor supplies several experimental stations with neutron flux (hot, thermal or cold neutrons). The NeXT station (used here) is supplied by a flux of up to 1.4 E10 n/cm2/s of cold neutrons. A medium resolution detector allows the neutron imaging. It is composed of a scintillator, a mirror and camera plus optics, X-rays are generated using a sealed source generator Hamamatsu L12161-07 X-ray microfocus generator) X-ray are monitored using a VarexScan® detector, equipped with a Cesium Iodide scintillator.

The main advantage of the dual beam is to benefit from different beam attenuation patterns [5, 9]. As hydrogen's neutron attenuation coefficient is very high compared to other materials used here, the Neutron contrast is mainly sensitive to the water saturation. X-ray contrast however is sensitive to both water saturation and salt content.

The main parameters for radiography acquisitions are: X-ray pixel resolution of 40 μm; Neutron pixel resolution of 15 μm; acquisition time of 8s for both beams. Using this configuration, the resulting X-ray attenuation map appears to be noisier than the Neutron one. The 2D Neutron and X-ray projections are pre-processed in order to allow further quantitative computations. First, the Neutron projections are down-scaled by a factor of 0.375 (=15 μm/ 40 μm) to match the X-ray projection pixel resolution. Then, the Neutron and the X-ray projections are registered to have the two sets of projections spatially aligned. It shall be reminded that the two beams are hitting the core sample from a different angle (see **Fig. 4**), the sample is not rotated during the monitoring. Therefore the two sets of projections are not showing the same 2D view of the core (especially in the radial direction). This effect is mitigated when considering the mean value (2D projection averaged on the whole sample range) or the vertical profile (2D projection averaged in the radial direction). Finally, the natural logarithm is applied to all projections.
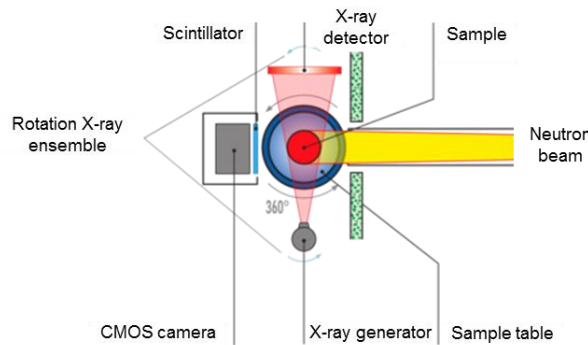

Fig. 4: Schematized top view of the NeXT dual beam lines (modified from [9]).

For both beams, the relation between intensity attenuation and the materials crossed can be expressed using the Beer-Lambert law [11]. For a multi-component system, it can be written as (1):

$$I(t) = I_o e^{-\sum \mu_i x_i} \quad (1)$$

Where $I(t)$ and I_0 respectively refer to the transmitted and incident ray intensity, μ_i and x_i are respectively the material i attenuation coefficient and linear path of material i crossed by the beam. The summation operation $\sum$ applies for all material crossed between the source and the detector, including all the cell components, the rock sample and the fluids saturating the rock. All constant quantities can be gathered and lumped in the incident ray intensity. In these experiments, three material paths are changing through time namely deionized water, nitrogen and salt. For all computations, the following simplifying hypothesis are made: (i) The KBr salt has the same attenuation coefficient when at solid or dissolved state and (ii) X-ray attenuation is linear to the salt quantity. With these hypotheses, the intensity attenuation $I(t)$ can be expressed for both beams as follow (2):

$$I(t) = I'_o e^{-\sum \mu_{H_2O} x_{H_2O} + \mu_{KBr} x_{KBr} + \mu_{N_2} x_{N_2}} \quad (2)$$

$$with \; I'_o = I_0 e^{-\alpha}$$

Where α account for the set-up constant contribution to the beam attenuation. The conservation of the total length path X of material crossed allows to write equation 3:

$$x_{H_2O} + x_{N_2} + x_{KBr} = X \quad (3)$$

As the natural logarithm is applied on all projections during the pre-processing, equation 2 become:

$$\log[I(t)] = \log[I'_0] - \sum_{N_2, H_2O, KBr} \mu_i x_i \quad (4)$$

Equation 4 needs to be calibrated for both beams to characterize the attenuation coefficients of all materials. It can be easily conducted for μ_{H2O} and μ_{N2} by saturating the sample with deionized water and nitrogen. However, the salt coefficient μ_{KBr} cannot be directly measured using its pure phase (solid salt), but its contribution on the Neutron and X-ray intensities attenuations can be estimated using a mixture: the 100g/L KBr brine (referred as the C_0 brine). This solution allows to calibrate the attenuations for a pore volume filled with 31mg of KBr salt (C_0*PV) and the remaining space by deionized water ($\mu_{C0}*X = x_{KBr}*\mu_{KBr} + \mu_{H20}*x_{H2O}$, with $x_{KBr} + x_{H20} = X$). Its comparison with the Neutron and X-ray values recorded with the deionized water will allow to determine the contribution of the salt alone.

The calibration of both beams is conducted with the following injection sequence:
1- The sample is initially dried and saturated with N_2.
2- It is saturated with deionized water (see details in section 2.3)
3- It is then saturated with the C_0 brine using miscible displacement.
4- Nitrogen is injected in the brine. Only the first steps are recorded during the viscous drainage, before the water evaporation starts, changing the brine concentration.

The mean Neutron and X-ray intensities monitored during the calibration are displayed in **Fig. 5**. The two signals variations are normalized between the dry state (N_2 saturated, reached at the end of step 1) and saturated with the C_o brine (C_0 saturated, reached at the end of step 3). Equation 4 can be written for both beams for these two chosen references, giving respectively:

$$\log[I(N_2)] = \log[I'_0] - \mu_{N_2} X \quad \text{(when } N_2 \text{ saturated)}$$

$$\log[I(KBr)] = \log[I'_0] - \mu_{C_0} X \quad \text{(when } C_0 \text{ saturated)}$$

With the normalization, equation 4 becomes:

$$\frac{\log[I(t)] - \log[I(C_0)]}{\log[I(N_2)] - \log[I(C_0)]} = \frac{\mu_{C_0} X - \sum_{N_2, H_2O, KBr} \mu_i x_i}{X(\mu_{C_0} - \mu_{N_2})} \quad (5)$$

All projections (Neutron and X-ray) are processed with the operations described by equation 5. The values obtained after this processing are no longer intensities. They neither express a saturation, as the sample saturation evolves between more than two phases. They are referred in the rest of the text as the X-ray and the Neutron-ray values. In this system of normalization, the X-ray and the Neutron-Ray values are both set to 0 when the sample is saturated with C_0 brine ($x_{C_0} = X$) ; and to 1 when it is dry ($x_{N_2} = X$). The question that remains is how these values behave when the brine salinity is changed (lower or higher salinities).

The normalization described above is used for all next graphical representations. The cross-plot (**Fig. 5**) shows the Neutron and X-ray values for our three references phases: the nitrogen, the deionized water and the C_0 brine. Their coordinates (in this system of normalization) are given on the plot. All the points between these poles are recorded during the phase replacement. They show a perfect linear evolution from pole to pole. The positions of the poles confirm that the Neutron attenuation is mainly sensitive to water (because of the hydrogen). However, there is a small variation between deionized water and C_0 brine: C_0 brine attenuates slightly less the Neutron than the deionized water. It might be explained by an effect of dilution of the water molecules by the ionic species dissolved in the brine. For the X-ray, both the salt and the water attenuate the beam: the attenuation measured between the N_2 phase and the C_o phase is caused at 36% by the water molecules and at 64% by the dissolved salt.
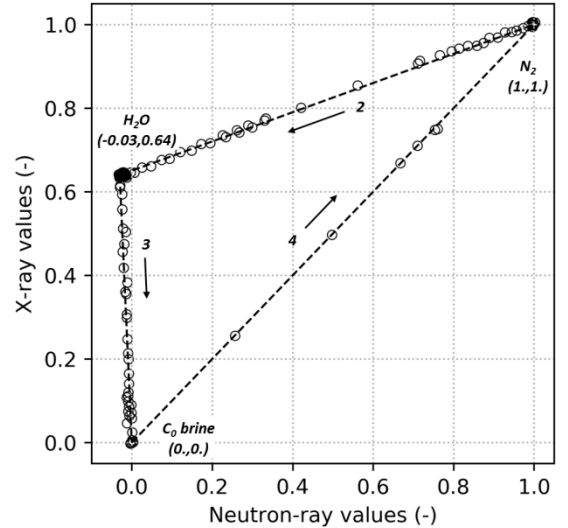

Fig. 5 : Scatter plot of X-ray and Neutron-ray values during the calibration experiment. Arrows indicate the injection sequences described in the text. X-ray and Neutron-ray values are obtained with equation 5.

These poles and vectors that connect them draw a two axes plot that enables to compute the gas saturation Sg, the salt quantity m_{KBr} and the brine concentration C_{KBr} from the Neutron and X-ray values. These axes are drawn in **Fig. 6**. The green axis expresses the gas saturation, the blue axis expresses the salt quantity (1 unit = 31mg, the quantity of salt contained in one PV of Co brine). The grey diagonals give the brine concentration, in C_0 unit. An example is given in **Fig. 6** with a Neutron and X-ray measurement (see the

red marker) that records the saturation process, half-way through, of the dry sample with a 50g/L KBr brine ($C_0/2$ brine). The marker projection on the saturation axis gives the gas saturation: $Sg = 0.5$; its projection on the salt axis give the quantity of salt: ¼*31mg = 0.8mg; and the grey diagonal the marker fall on gives the brine concentration: $C_0/2$.

The previous calculus strictly applies only when all the salt is dissolved in the brine phase. A correction is made when salt precipitates. Its effect on X-ray attenuation is considered to be the same, following the hypothesis made above, but its effect on the Neutron attenuation is different. When the salt is dissolved in the brine phase, it alters the density of water molecules and causes the reduction of attenuation described above. When the salt is in solid state, a third phase is formed. It still attenuates the X-ray, but no longer alters the brine phase (and no longer affect the Neutron-ray). The volume it occupies is computed using a salt density of 2.16g/cc. The reduction of porosity caused by the salt precipitation could then be estimated using equation 6.
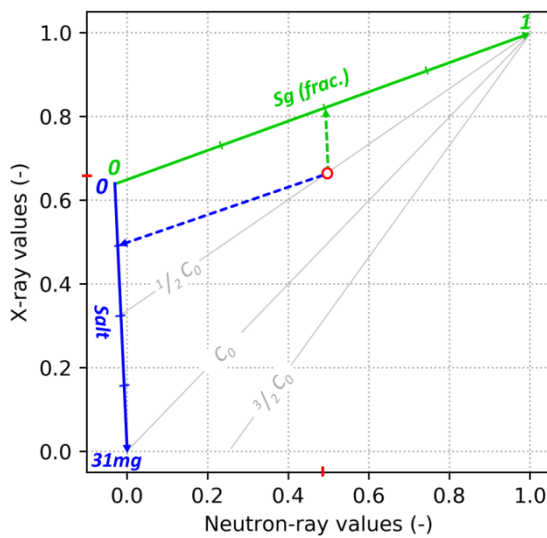
$$\phi = \frac{m_{KBr}^{solid}}{\rho_{KBr}*PV} \quad (6)$$

Fig. 6: Illustration of gas saturation, salt quantity and brine concentration computations from a Neutron and X-ray measurements (red marker). Explanations are given in the text.

3 Results and discussion

The four tests are presented and interpreted successively. They have been conducted one after the other, in the same acquisition sequence, without interrupting the X-ray and Neutron beams. As mentioned in the introduction, the two first tests aimed to calibrate the dual beam monitoring method.

3.1 Dry-out with the deionized water

Deionized water is used for this preliminary experiment. In these conditions, the Neutron and X-ray beams are expected to show the same trend when normalized between the dry

and the saturated states. The Neutron and X-ray attenuations are plotted in **Fig. 7** with the mass flow rate. The protocol described in section 2.3 is applied: the sample is saturated with the water from t = 0 to t = 14min). The gas injection starts at t = 14min, the gas inlet pressure is set to 0.55bars. The 1D vertical profiles recorded during the dry-out (from t = 14min to t = 28min) are displayed in **Fig. 8**.

The gas saturation during the dry-out shows the variation steps already described in previous works [1, 3]. We observe a viscous gas drainage to Swi (until t = 17min) followed by the evaporation of the remaining trapped brine. The Swi value can be estimated at 20% from these plots. In **Fig. 8**, a front is observed during the evaporation with only a small production of water ahead of the front (the gas saturation plateau ahead of the front increase from 72% to 82% during the front advancement). Different mechanisms can explain this production ahead of the front (drainage, evaporation or a small capillary back flow), and will be discussed later. Globally, the evaporation process is quick enough to prevent the capillary forces to re-distribute the water in the sample.
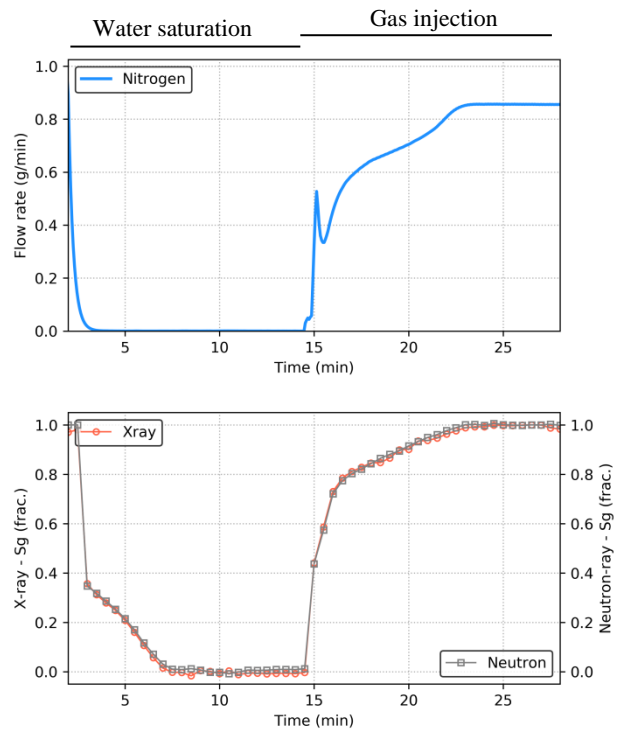

Fig. 7 : Dry-out with deionized water. X-ray and Neutron beams are normalized between dry state and saturated with deionized water.
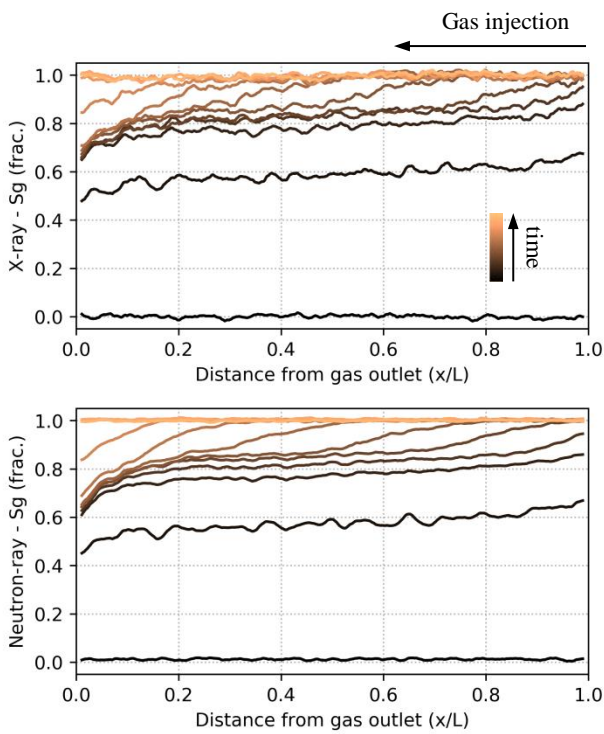
Fig. 8 : X-ray and Neutron-ray profiles during the dry-out with deionized water (from t = 14min to t = 28min). X-ray and Neutron beams are normalized between dry state and saturated with deionized water. Gas is injected from the right.

Fig. 9: Dry-out with the 100g/L KBr brine. At t = 45min, the sample is saturated with deionized water before being replaced by the KBr brine.

3.2 Dry-out with the KBr brine

The previous experiment is reproduced with the deionized water replaced by the 100g/L KBr brine. The same gas inlet pressure of 0.55bars is set. The Neutron and X-ray attenuations are plotted in **Fig. 9**. In this experiment, the two attenuation curves are not superimposed due to the addition of salt. The quantity of salt and the gas saturation are computed in blue and green using the method detailed in section 2.4. The deionized water replacement by the KBr brine is recorded from t = 45min to t = 65min. The gas injection starts at t = 66min. Pollutions with deionized water occur between t = 55min to t = 65min.

The salt mass curve shows an increase from 0 to 1unit during the replacement of deionized water by the KBr brine. Here, 1unit is defined as 31mg, the quantity of salt contained in a PV of C_o brine. This normalization allows to read the fraction of the initial quantity of salt that remained trapped in the sample during the dry-out. The dry-out dynamic is similar to the previous experiment, exhibiting the same steps: (1) the viscous drainage during which the salt is produced with the water and (2) the water evaporation during which salt is left in the sample. The second step is detected when the Neutron and X-ray attenuations divert. The quantity of salt left in the core at the end of the dry-out allows to quantify the contribution of the two production mechanisms (drainage and evaporation) to the water production. Here, we observe that 20% of the initial salt remain in the sample at the end of the experiment (cf. blue curve on **Fig. 9**). This is in agreement with the Swi value that was estimated at the end of the drainage with deionized water.
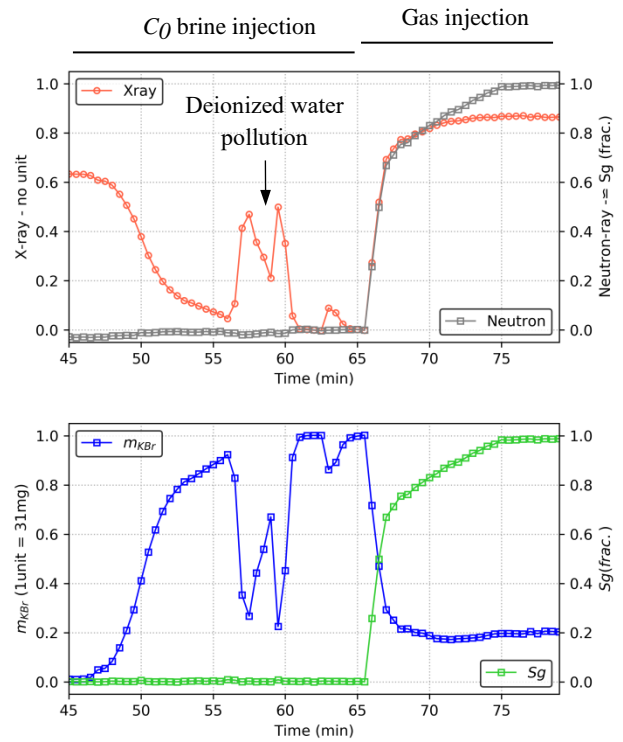
The 2D projections recorded at the end of the dry-out are given in **Fig. 10**. They clearly show a small horizontal salt bank on the X-ray projection, close to the gas outlet. The salt distribution profiles recorded at Swi (dissolved in the brine) and at the end of the dry-out (precipitated in the sample) are compared in **Fig. 11**. The dissolved salt distribution shows that the capillary end-effect locally increases the quantity of salt. The edges of the sample (1 mm from each side) are cropped during the data processing. It hides the extent of the end-effect and the dissolved salt it contains. The precipitated salt curve shows a salt deposition all along the core, with an accumulation close to the outlet. It is partly explained by the initial dissolved salt distribution at Swi and probably also by a small redistribution of the salt contained in the capillary end-effect. However, if we exclude the capillary end-effect zone, the two curves show a perfect superposition, suggesting no water reorganization during the evaporation. The water production that was observed ahead of the front during the first experiment shall therefore be explained by early evaporation. All others production mechanisms (drainage or capillary back flow) would have redistributed the salt.
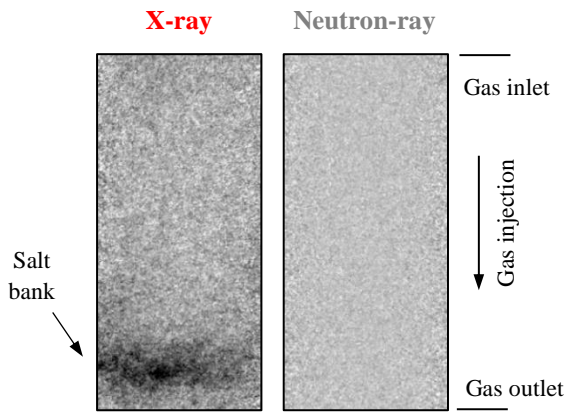
X-ray **Neutron-ray**

Gas inlet

Gas injection

Salt bank

Gas outlet

Fig. 10: 2D projections at the end of the dry-out (no capillary contact), when initially saturated with the KBr brine. On the X-ray projection, darker shades suggest salt bank position The Neutron-ray projection shows a flat profile confirming that the sample is dry.
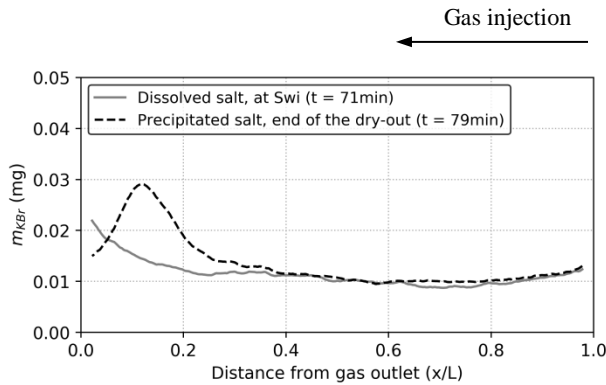
drainage (t = 95min, blue curve). After that, the quantity of salt is multiplied by 4, from 0.2 units to 0.8 units (corresponding to 25mg). This demonstrates a substantial salt accumulation in the sample, while only gas is injected through it. During this salt accumulation sequence, we observe a strong decrease of the gas flow rate. This is easily explained by a reduction of the initial sample permeability as salt precipitates in the porous-space [1, 2]. The reduction of porosity caused by salt deposition will be estimated using the Neutron and X-ray profiles.

2D projections recorded before the salt starts to accumulate are showed in **Fig. 13**. They show a comparable small salt bank formed close to the gas outlet, as observed when no capillary contact was maintained (**Fig. 10**). However, in this experiment, the Neutron projection clearly shows that the bottom of the sample remains partially saturated with water. This behavior is obviously due to the imposed capillary contact boundary condition.
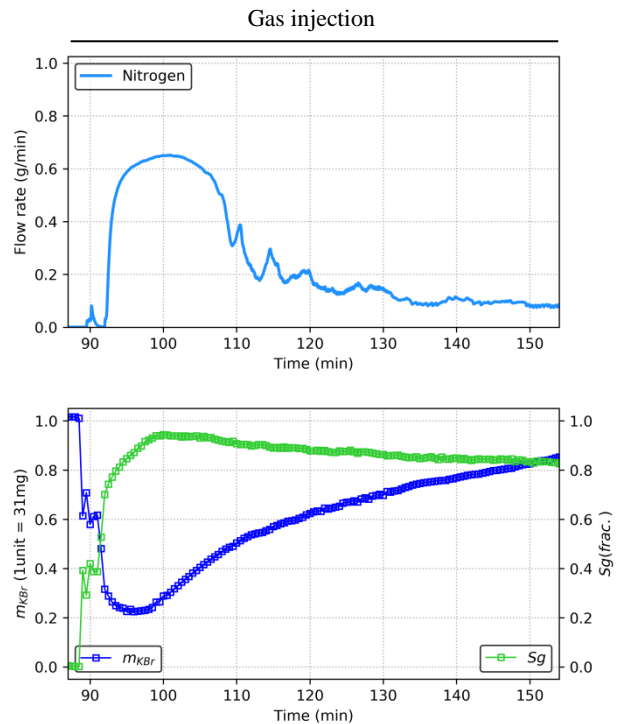

Gas injection

Fig. 11: Salt distribution, dissolved in the brine at Swi (plain curve) and precipitated at the end of the dry-out (dashed curve).

3.3 Dry-out with capillary contact

The dry-out with the KBr brine is reproduced with a capillary contact maintained at the gas outlet using the bottom inlet and outlet lines (see **Fig. 3**). A recent work [1] has suggested that the capillary contact acts as a salt pump, allowing to accumulate more salt in the sample than initially dissolved. The underlying mechanism is believed to be a competition between evaporation and capillary forces [3]. The effect of the gas flow rate on this equilibrium is studied: the experiment is conducted twice with the inlet pressure set to 0.55bars and 0.35bars. These two configurations are referred to high and low pressure gradient dry-out, respectively.

3.3.1 High pressure gradient

For this dry-out experiment the inlet gas pressure is set to 0.55 bars. The gas is injected in the sample initially saturated with the 100g/L KBr brine. The gas flow rate during the dry-out is given in **Fig. 12**, with the gas saturation in green and the computed salt quantity in blue.

The initial steps of the dry-out exhibit a similar behavior as previously seen (i.e. a drainage step followed by the evaporation steps). The Swi value can be estimated to 20%, from the minimum salt quantity trapped after the

Fig. 12 : Dry-out with the 100g/L KBr brine and a capillary contact maintained at the gas outlet (high pressure gradient case).

X-ray   Neutron-ray

Gas inlet

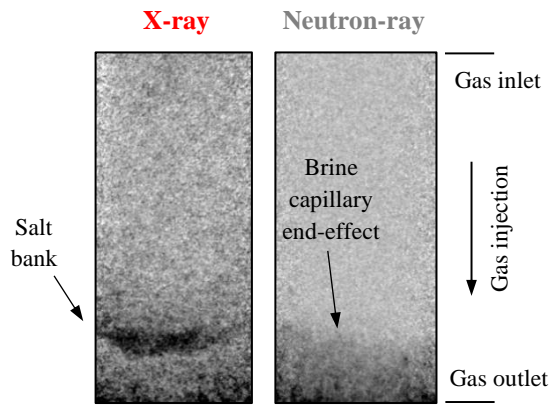Brine capillary end-effect

Gas injection

Salt bank

Gas outlet

Fig. 13: 2D projections at the end of the dry-out (before the salt accumulation t = 95min), when initially saturated with the KBr brine (dry-out with a capillary contact). On the X-ray projection, darker shades suggest salt bank position. On the Neutron-ray projection, darker shades suggest higher water saturations.

The evolution of the initial small bank during the dry-out is showed in **Fig. 14**. The 2D projections show a rise of both the salt bank and the water front in the sample. The evolution visible on the X-ray projections suggests an evolution in two steps: first the salt bank is getting quickly wider and thicker while staying at same height, and secondly, from t = 107 min, it starts migrating upward in the core while slowly getting wider. During the first step, salt accumulation results in substantial gas flow rate reduction (almost 50%). Afterward, we observe a stick and slip like behavior of water and salt rises.
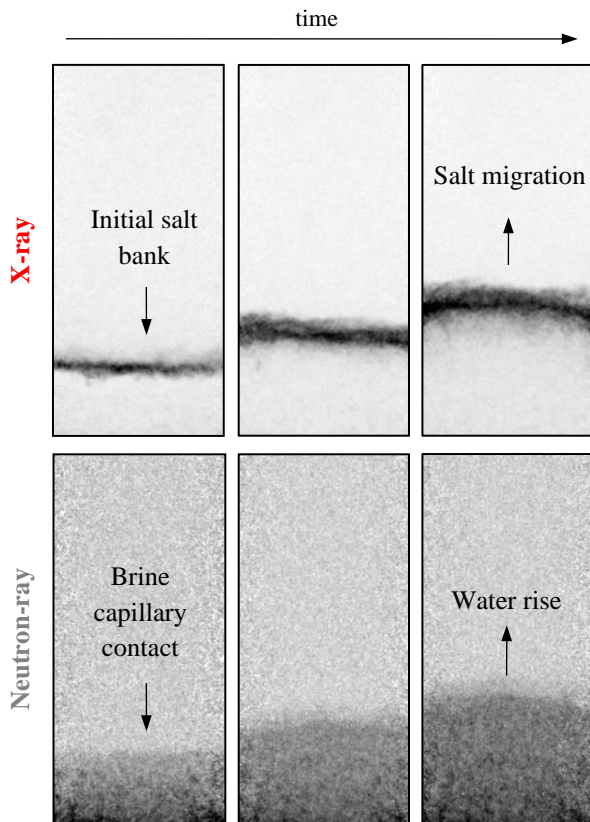
time

X-ray

Initial salt bank

Salt migration

Neutron-ray

Brine capillary contact

Water rise

Fig. 14: 2D projections during the salt accumulation, taken at 100 min, 120 min and 140 min from left to right. Gas is injected from the top. On the X-ray projections, darker shades suggest salt bank

position. On the Neutron-ray projections, darker shades suggest higher water saturations.

The brine saturation Sw, the brine concentration C_{KBR} and the precipitated salt m^{solid}_{KBR} profiles are given in **Fig. 15** for different time steps during the salt accumulation. The profiles give meaningful insight to understand the mechanism of salt accumulation and rising. In this work, we consider that salt precipitates instantaneously once the solubility limit of $6.5*C_O$ is reached excluding any super-saturation condition. Actually, the salt only precipitates when two conditions are met: Sw > 0 and $C_{KBr} = 6.5*C_O$. The brine saturation and the KBr concentration profiles show that the capillary contact maintained almost constant boundary conditions at the gas outlet which prevents salt precipitation at the outlet. The brine concentration, however, quickly rises to its limit of solubility ($6.5*C_O$) at few mm from the gas inlet, where salt starts to precipitate. The brine saturation profiles show that the sample is completely dry behind the salt bank. A residual value can be read on these curves, around 2%. It can be attributed to the X-ray and Neutron-ray signals calibration. The precipitated salt curves clearly show the salt bank migration toward the gas inlet and its thickening during its displacement. Following the previous remarks, the salt migration can be explained by the water front displacement that carries more salt and allows salt to precipitate higher in the sample.

The reduction of porosity is computed from the precipitated salt curves (cf. equation 6) and it is directly proportional to the precipitated salt quantity. The apparent migration of the salt starts when the local porosity is reduced by up to approximately 13-15% in some section of the sample. At the end of the experiment (at t = 155min), some sections of the sample show a reduction of the pore space by up to 20%. This relatively moderate porosity reduction induces an average flow rate reduction by almost a ratio of 6 (cf. maximum to minimum ration of flow rate in **Fig. 12**). This observation supports the hypothesis of a preferential salt precipitation along the pore wall plugging by the throats between pores.
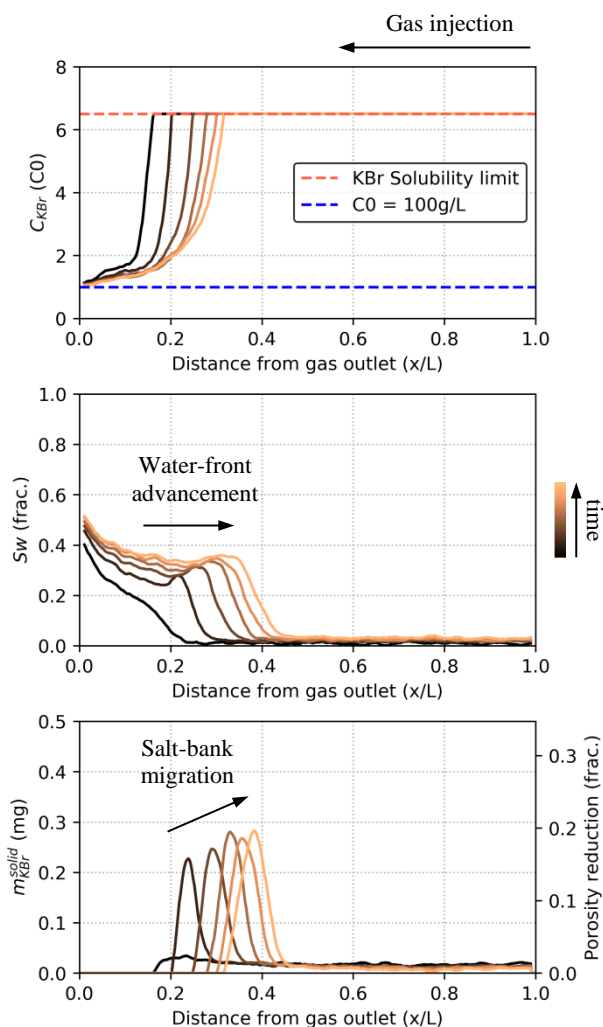
Fig. 15: Brine concentration C_{KBr}, brine saturation Sw and precipitated salt profiles m^{solid}_{KBr} profiles computed during the salt accumulation. The reduction of porosity is estimated from the m^{solid}_{KBr} curves. Profiles are computed regularly from t = 100min to t = 150min.

These different curves are plotted for a single time step on the same plot in **Fig. 16**. It shows the relation between the salt bank and the brine phase. The section where salt precipitates is saturated by both the gas and the brine. The presence of these two phases is actually required to allow the precipitation. The salt bank doesn't act as a barrier for the brine. It is in constant rise in the sample by capillary forces, but the height reached by the front is limited by its evaporation. If deionized water had been used, the height reached would have quickly stabilized. Here, the evaporation is causing salt to precipitate. As it accumulates in the pore-space, the porosity is reduced and the gas flow rate decreases (**Fig. 12**), changing the equilibrium between capillary forces and evaporation speed. The decrease of the gas flow rate allows the water to imbibe higher in the sample. Salt precipitates ahead the previous bank while its rear back is dissolved by under-saturated brine.

The curves plotted in **Fig. 16** show the equilibrium of the different phases for specific injection conditions. The brine phase is not breaking-through the sample, suggesting flowing conditions close to null. From t = 100min to t = 150min, the water saturation is increased by 9% by capillary rise, corresponding to an average flow rate of 33µl/h. Yet, this flow rate is not high enough to explain the rate of salt

accumulation in the sample. Indeed, the brine is constantly evaporating in the gas, and it is compensated by an additional brine pumping through the capillary contact. This additional contribution is estimated using the salt mass curve to an average of 190µl/h between t = 95min to t = 150min. It is twice more important during the early stages of the dry-out. Despite the brine saturation profiles being close to static, the brine flow rate is far from being null. It explains how the rear back of the salt bank is quickly dissolved while the brine slowly rises.
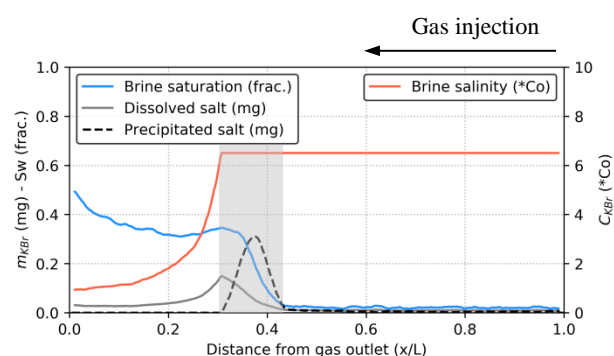

Fig. 16: Salt repartition in the different phases during the dry-out with capillary contact (t = 150min). The gray area shows where the conditions for salt precipitation are met.

3.3.2 Low pressure gradient

For the second dry-out experiment with capillary contact, the inlet gas pressure is set to 0.35bars. The gas is injected in the sample initially saturated with the 100g/L KBr brine. The gas flow rate during the dry-out are given in **Fig. 17**, with the gas saturation in green and the salt quantity in blue.

The early phases of the dry-out are again comparable to what has been reported previously. The initial salt bank is formed at halfway-up the sample, higher than in the previous experiment. This is consistent with the lower inlet pressure allowing the capillary forces and the brine evaporation to equilibrate higher in the sample.

The next steps of the dry-out demonstrate a completely different behavior than previously observed, with the gas flow rate showing alternating phases of draw-down and build-up (see phases referred as 1 and 2 in **Fig. 17**). The gas saturation is correlated to these variations: the higher the gas flow rate, the higher the gas saturation. During the draw-down phases, the gas flow rate is reduced by 10 times its initial value (from 0.25g/min to 0.025g/min), while the total quantity of salt in the sample is increasing monotonously. The quantity of salt dissolved in the brine and the quantity of salt precipitated in the sample are also displayed in **Fig. 17** in red and black respectively. These two curves demonstrate the same alternating cycles of build-up and draw-down, yet inversely correlated. Indeed, during a gas draw-down, the quantity of precipitated salt decreases while the quantity of dissolved salt in the brine phase increases, and conversely during a gas build-up. These curves suggest the phases of gas draw-down and build-up are controlled by cycles of salt precipitation and salt dissolution.
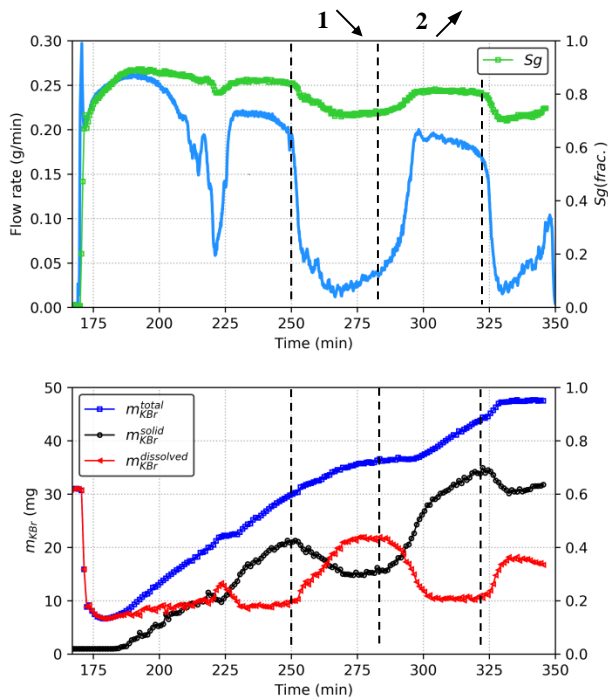
Fig. 17: Dry-out with the 100g/L KBr brine and a capillary contact maintained at the gas outlet (low pressure gradient case). The two sections noted 1 and 2 shows a cycle of gas draw-down and gas build-up.

The 2D X-ray projections recorded during draw-down and build-up phases are given respectively in **Fig. 18** and **Fig. 20**. The corresponding precipitated salt profiles computed for different time steps are given in **Fig. 19** and **Fig. 21**, for the draw-down and the build-up respectively.

As seen earlier, the gas draw-down is initiated by a strong reduction of the porosity in a limited section of the core. For the draw-down described here, the porosity is reduced by up to 30% (see **Fig. 19**). This allows first the brine to rise in the sample while dissolving the rear back of the salt bank and then the salt to precipitate higher in the sample. These steps are clearly visible on the 2D X-ray projections (**Fig. 18**). The quantity of salt dissolved is balanced by the quantity of salt that precipitates. The total quantity of salt is still showing an increase due to the rise of the water in the sample, pumping additional dissolved salt through the capillary contact. The major difference with the previous dry-out experiment is that a second salt bank is formed while a unique one was observed previously. This difference is crucial as it triggers the gas build-up cycle: the formation of a second salt bank globally spreads the salt in a less damaging configuration for the permeability. This is well understandable in **Fig. 19**: the maximum of porosity reduction falls from 30% to 20% during the formation of the second bank. The gas flow rate quickly increases following this, initiating the gas build-up.
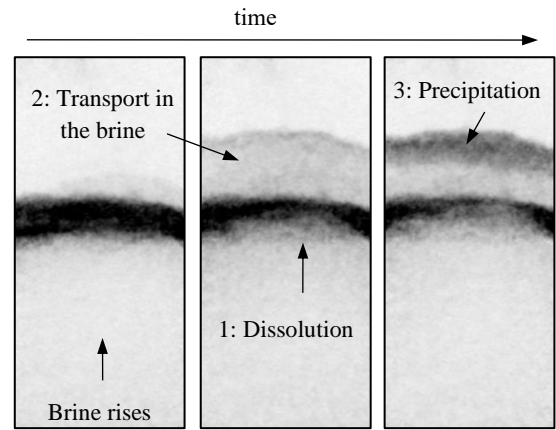

Fig. 18: 2D X-ray projections during a gas draw-down (see cycle 1 in **Fig. 17**), taken at 250 min, 265 min and 280 min from left to right. Gas is injected from the top. On the X-ray projections, darker shades suggest salt bank position.
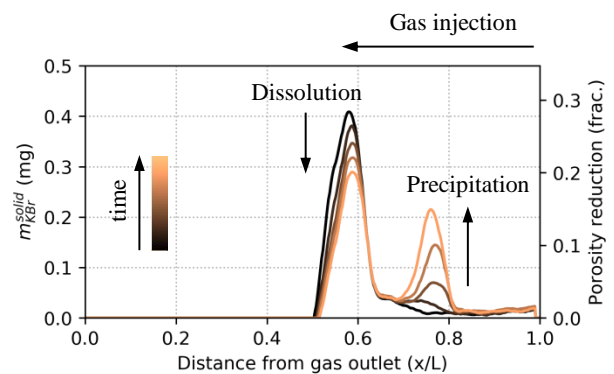

Fig. 19: Precipitated salt profiles during a gas draw-down (see cycle 1 in **Fig. 17**).

During the gas build-up, the water withdrawn from the sample, and no salt dissolution is observed. As a matter of fact, the newly formed salt bank is left ahead of the water-front, where the sample is dry and only salt precipitation is observed during this phase. This is clearly visible on the salt profiles in **Fig. 21** and on the 2D projections given in **Fig. 20**. It is during these phases of gas build-up that the quantity of salt in the sample increases the most. The porosity is strongly reduced again during this step and consequently triggers the next gas draw-down phase.
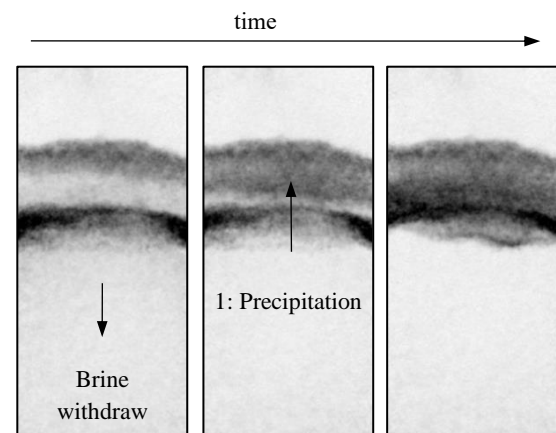

Fig. 20: 2D X-ray projections during a gas build-up (see cycle 2 in **Fig. 17**), taken at 280 min, 300 min and 320 min from left to right. Gas is injected from the top. On the X-ray projections, darker shades suggest salt bank position.
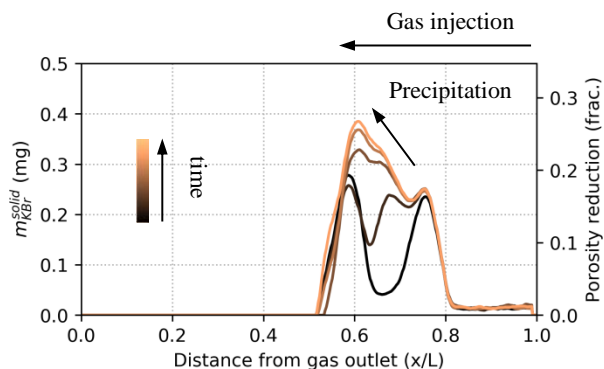
Fig. 21: Precipitated salt profiles during a gas build-up (see cycle 2 in **Fig. 17**).

4. Conclusion

The dual beams monitoring technique has demonstrated a real contribution to study the salt precipitation dynamic induced by gas flow-through drying. The difference of attenuation pattern between the Neutron and the X-ray beams is used to de-correlate beam attenuations caused by the water and the salt. A method to calibrate and process the two signals has been presented, allowing to separately quantify the different phase saturations and brine salinity as well as the reduction of porosity caused by the salt deposition. This information is crucial to better calibrate numerical models and particularly the permeability reduction with salt precipitation.

Results of four dry-out experiments monitored with this method are presented here. The two first experiments mostly aimed to calibrate the dual monitoring for the different phases. The last two experiments have been conducted with a brine capillary contact maintained at the gas outlet. Experimental data have given new insight to understand the organization of the three phases (the brine, the gas and the precipitated salt) when a salt bank is formed in the sample. The quantity of salt that accumulates allows to estimate the flow rate of brine pumped through the capillary contact to compensate for the brine evaporation in the gas phase. The observations have shown that a reduction of the initial porosity in some section of the sample by 13-15% was enough to trigger a gas draw-down, characterized by the migration of the salt toward the gas inlet. The rise of the salt bank involves three steps: salt dissolution, salt transport in the brine phase and salt precipitation where the water front stabilizes. In some conditions (low gas pressure gradient for example), the rise of the water can be fast enough to form a second salt bank higher in the sample. It has been observed that the formation of the second salt bank could spread the precipitated salt in a less damaging configuration for the gas flow, triggering a phase of gas build-up characterized by the withdrawal of the water. These phases of gas draw-down and build-up can alternate until the sample clogging.

Future works can include:
- The construction of a permeability reduction curve as a function of the porosity reduction.
- The evaluation of the thermodynamic aspect of the drying, especially the water vapor concentrations.

References

[1] O. Lopez *et al.,* "Permeability alteration by salt precipitation: Numerical and experimental investigation using X-Ray Radiography," *E3S Web Conf.*, vol. 146, A, p. 3001, 2020, doi: 10.1051/e3sconf/202014603001.

[2] Y. Peysson, B. Bazin, C. Magnier, E. Kohler, and S. Youssef, "Permeability alteration due to salt precipitation driven by drying in the context of CO2 injection," *Energy Procedia*, vol. 4, pp. 4387–4394, 2011, doi: 10.1016/j.egypro.2011.02.391.

[3] Y. Peysson, L. André, and M. Azaroual, "Well injectivity during CO2 storage operations in deep saline aquifers—Part 1: Experimental investigation of drying effects, salt precipitation and capillary forces," *International Journal of Greenhouse Gas Control*, vol. 22, pp. 291–300, 2014, doi: 10.1016/j.ijggc.2013.10.031.

[4] L. André, Y. Peysson, and M. Azaroual, "Well injectivity during CO2 storage operations in deep saline aquifers – Part 2: Numerical simulations of drying, salt deposit mechanisms and role of capillary forces," *International Journal of Greenhouse Gas Control*, vol. 22, pp. 301–312, 2014, doi: 10.1016/j.ijggc.2013.10.030.

[5] T. Giorgis, M. Carpita, and A. Battistelli, "2D modeling of salt precipitation during the injection of dry CO2 in a depleted gas reservoir," *Energy Conversion and Management*, vol. 48, no. 6, pp. 1816–1826, 2007, doi: 10.1016/j.enconman.2007.01.012.

[6] J. Mahadevan, M. M. Sharma, and Y. C. Yortsos, "Flow-through drying of porous media," *AIChE J.*, vol. 52, no. 7, pp. 2367–2380, 2006, doi: 10.1002/aic.10859.

[7] J. Mahadevan, M. M. Sharma, and Y. C. Yortsos, "Water removal from porous media by gas injection: Experiments and simulation," *Transport in Porous Media*, vol. 66, no. 3, pp. 287–309, 2007, doi: 10.1007/s11242-006-0030-z.

[8] D. Le, H. Hoang, and J. Mahadevan, "Impact of Capillary-Driven Liquid Films on Salt Crystallization," *Transport in Porous Media*, vol. 80, no. 2, p. 229, 2009, doi: 10.1007/s11242-009-9353-x.

[9] A. Tengattini *et al.,* "NeXT-Grenoble, the Neutron and X-ray tomograph in Grenoble," *Nuclear Instruments and Methods in Physics Research Section A: Accelerators, Spectrometers, Detectors and Associated Equipment*, vol. 968, p. 163939, 2020, doi: 10.1016/j.nima.2020.163939.

[10] Florian Grünauer, "Design, optimization, and implementation of the new neutron radiography facility at FRM-II," 2005. [Online]. Available: https://pdfs.semanticscholar.org/041f/fe1ef9477759f231bd46224240ef152141d7.pdf

[11] P. Rinard, "Neutron interactions with matter," *Passive Nondestructive Assay of Nuclear Materials*, pp. 375–377, 1991.